

Article

Application of A Novel, Non-Doped, Organic Hole-Transport Layer into Single-Walled Carbon Nanotube/Silicon Heterojunction Solar Cells

Tom Grace ¹, Hong Duc Pham ², Christopher T. Gibson ^{1,3,4} , Joseph G. Shapter ^{1,5} 
and Prashant Sonar ^{2,*}

¹ College of Science and Engineering, Flinders University, 5042 Adelaide, Australia; tom.grace@flinders.edu.au (T.G.); christopher.gibson@flinders.edu.au (C.T.G.); joe.shapter@flinders.edu.au (J.G.S.)

² Institute of Future Environment and School of Chemistry, Physics and Mechanical Engineering, Queensland University of Technology (QUT), 2 George Street, 4001 Brisbane, Australia; h22.pham@qut.edu.au

³ Flinders Institute for NanoScale Science and Technology, College of Science and Engineering, Flinders University, 5042 Adelaide, Australia

⁴ Flinders Microscopy and Microanalysis, College of Science and Engineering, Flinders University, 5042 Adelaide, Australia

⁵ Australian Institute for Bioengineering and Nanotechnology, The University of Queensland, 4072 Brisbane, Australia

* Correspondence: sonar.prashant@qut.edu.au

Received: 6 October 2019; Accepted: 30 October 2019; Published: 5 November 2019



Abstract: The search for novel solar cell designs as an alternative to standard silicon solar cells is important for the future of renewable energy production. One such alternative design is the carbon nanotube/silicon (CNT/Si) heterojunction solar device. In order to improve the performance of large area CNT/Si heterojunction solar cells, a novel organic material, 4,10-bis(bis(4-methoxyphenyl)amino)naphtho[7,8,1,2,3-nopqr]tetraphene-6,12-dione (DPA-AN interlayer) was examined with SEM and AFM imaging to determine an optimal thickness for solar cell performance. The DAD was shown to improve the device performance with the efficiency of large area devices improving from 2.89% ± 0.40% to 3.34% ± 0.10%.

Keywords: solar cells; hole transport layers; organic conductors; thin films

1. Introduction

As the issues with fossil fuel-based methods of energy production become more and more obvious and pronounced, the push to improve environmentally friendly methods of energy generation becomes critically important. In the world of solar energy, one emerging design is the carbon nanotube/silicon (CNT/Si) heterojunction solar cell. This architecture was first studied in 2006 [1] with a percent current efficiency (PCE) of 1.3% and this has been improved considerably from there with PCEs as high as 17% [2] reported by Wang et al. in 2015. Many different methods have been employed to improve this cell design, with different surface architectures, and different nanotube types (SWCNTs, DWCNTs and MWCNTs as well as different SWCNTs chiralities). Of particular interest is the flourishing field of adding a thin interlayer between the silicon substrate and the CNTs in order to improve conductivity [3], act as an electron blocker [4], act as a hole transporter [4], and improve cell stability, or a combination of these effects. Several interlayers have been studied, including conductive polymers such as PEDOT:PSS, polyaniline (PANI), and P3HT [5]. Additionally, layers derived from other solar cell architectures have been employed such as the solid-state hole transporting material (HTM) 2,2',7,7'-tetrakis(N,N'-di-*p*-methoxyphenylamine)-9,9'-spirobifluorene, more commonly known

as spiro-OMeTAD, [6] which is the most commonly used interfacial HTM currently employed in perovskite-based solar cells. [7] Spiro-OMeTAD was found to improve the performance of CNT/Si cells [6]. However, there are downsides to the use of this material. First, the HTM requires a dopant to improve the conductivity to be used in a solar cell architecture and the effect of this dopant is not stable or long-lasting in ambient conditions [8]. Additionally, spiro-OMeTAD is a very expensive material limiting its use in large scale industrial procedures. Thus, it is important to search for cheaper materials which can be applied as alternative HTMs and do not require a degradable doping step, as well as furthering the search for HTMs with superior capabilities.

In the search for new HTMs one potential set of candidates involve anthanthrone dye-based systems. The molecule used in this research consists of the anthanthrone dye molecule (ANT) with two functionalized diphenylamine (DPA) end caps. Together the molecule is referred to hereafter as DPA-ANT-DPA. This molecule was synthesized by Pham et al. in 2017 for use as an HTM in perovskite solar cells [9]. The advantage of this molecule over more familiar chemical interlayers (such as Spiro-OMeTAD) is that DPA-ANT-DPA is cheaper and it does not require a dopant. The molecule has a donor-acceptor-donor structure and is produced via a one-step synthesis from relatively cheap components. Thus, DPA-ANT-DPA is a simpler and possibly longer lasting interlayer chemical than some other alternatives. This material, once dissolved in an organic solvent, can simply be coated onto a substrate in atmospheric conditions in order to produce a thin, dopant free, hole-transporting layer.

In the perovskite system, interlayer materials of this sort have been shown to provide similar benefits to device performance as Spiro-OMeTAD [9] with the advantage that the material can be prepared for spin coating in ambient conditions. Similar hole transporting materials have been applied to small area CNT/Si heterojunction devices [10]. These materials are 4,4'-(naphthalene-2,6-diyl)bis(*N,N*-bis(4-methoxyphenyl)aniline) (NAP), and (E)-4',4''-etene-1,2-diyl)bis(*N,N*-bis(4-methoxyphenyl)-[1'',1''']biphenyl]-4-amine) (BPV). Both were shown to produce small active area (0.079 cm²) CNT/Interlayer/Si devices with PCEs higher than 10% thanks to a reduction in recombination at the heterojunction interface.

The work reported in this paper focuses on the application of DPA-ANT-DPA (called DAD hereafter) (see Figure 1a) for large area CNT/Si solar cells. For large area cells, the challenge of moving the charge carriers over longer distances is of paramount importance to attain the best performance. For the CNT/Si system, methods to enhance the hole transport at the interface are central to ensuring the devices provide the best efficiency. The addition of the DAD as an interlayer between the CNTs and Si was shown to enhance the performance for the large area cells.

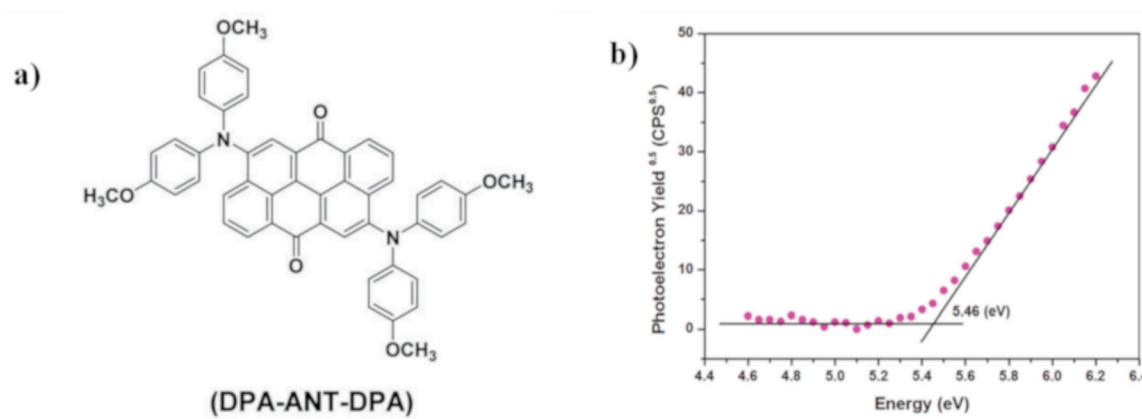


Figure 1. (a) The chemical structure of DAD (4,10-bis(bis(4-methoxyphenyl)amino)naphtho[7,8,1,2,3-nopqr] tetraphene-6,12-dione); (b) The photoelectron spectroscopy in air (PESA) of DAD.

2. Materials and Methods

2.1. DAD Preparation

Solid DAD is dissolved at a concentration of 60 mg in 1 mL of chlorobenzene and treated in an ultra-sonic bath for 30 min. The resultant mixture is filtered through a 45- μm pore filter to remove any remaining solid, leaving a deep green suspension.

2.2. CNT Preparation

Bath sonication preparation of suspensions was used in previously published work [10,11]. In brief, for the CNTs (Carbon Solutions Inc., Riverside, California), a surfactant solution was formed by adding Triton X-100 to water at a concentration of 1% v/v. This mixture was bath sonicated (≈ 50 WRMS (root mean squared Watts) (Elmasonic S 30 H)) for 20 min before dry CNTs were added to the mixture at a concentration of 1 mg mL⁻¹.

2.3. Graphene Oxide (GO) Synthesis

Graphene oxide was used to improve the strength of the SWCNT films. The synthesis method used was based on the paper by Marcano et al. [12]. In brief, a mixture of graphite flakes and KMnO₄ was prepared and an acidic solution made using a 9:1 ratio of H₂SO₄/H₃PO₄ was added. The mixture was heated to 50 °C and stirred for 12 h. After stirring, the reaction was cooled and poured onto ice made from purified water with 30% H₂O₂. The mixture was sifted to remove any remaining graphite and then centrifuged, with the solid material retained. This material was washed six times, twice with water, twice with 30% HCl, and twice with ethanol. The mixture was centrifuged after each wash. The remaining solid was filtered and vacuum dried overnight at room temperature, leaving dark grey graphene oxide flakes.

2.4. CNT and GO Suspension Preparation

CNTs and GO were mixed at a CNT:GO ratio of 2.25:1 in order to increase the strength of the CNT films. The carbon nanotube/graphene oxide (CNTGO) mixture was bath sonicated in four 20 min periods. The bath water was replaced after each period to keep the bath at around room temperature. Once the suspension was formed, it was centrifuged at 17,500 g for 1 h to remove material that was not well dispersed. The top 2/3 of the centrifuged mixture was collected and the remaining 1/3 was centrifuged for an additional hour to increase yield, with the top 2/3 collected. The centrifuge used was a Beckmann-Coulter Allegra X-22.

2.5. Solar Cell Substrate Preparation

Solar cell substrates were produced from purchased 100 mm thick silicon wafers with a grown 100 nm oxide surface layer which were cleaned in a mixture of 3:1 sulfuric acid and hydrogen peroxide. The wafers were then coated with a thin layer of AZ-1518 positive photoresist before being exposed to UV light through a patterned mask to create a photoresist pattern on the surface. The wafers were then sputter coated with a 5 nm layer of chromium, followed by a 445 nm layer of gold. The photoresist was removed in an acetone bath to produce gold patterned devices via a "lift-off" procedure. The rear contact was prepared by removing the 100 nm oxide layer from the rear of the wafer via etching with buffered oxide etch (BOE; 6:1 NH₄F:HF). The exposed silicon was allowed to sit in ambient conditions for 90 min before a 300 nm layer of aluminum was evaporated on to the wafer and was annealed for 30 min at 300 degrees.

The 1.5 cm \times 1.5 cm active area of each cell was prepared by etching the 100 nm oxide layer with BOE and then leaving the substrates to sit in air for 30 min.

2.6. DAD Film Deposition

The DAD solution is spin coated onto silicon substrates post BOE etch at various spin speeds for 30 s. A variety of deposition volumes and spin speeds were used to determine and ensure an optimal recipe to produce a good film.

2.7. CNTGO Film Production

CNTGO films were produced from suspension using vacuum filtration. A Buchner flask was attached to a water aspiration vacuum via tubing, and a glass frit was placed in the top with a rubber bung providing the seal. A series of two filter membranes were placed on the frit. The bottom membrane was a mixed cellulose ester (MCE) template membrane (VSWP, Millipore, 0.025 μm pore size). This membrane is patterned with the shape desired for the final film. The second (top) membrane is an MCE membrane (HAWP, Millipore, 0.45 μm pore size). A solution of approximately 250 mL of ultra-pure water containing an aliquot of CNTGO suspension was filtered through this setup. The flow rate of the solution was faster through the patterned hole in the lower membrane than through the 0.05 μm pores. Thus, the nanotubes/graphene oxide was deposited in the same pattern as the lower template paper. After the initial filtration an additional filtration of 250 mL of ultra-pure water was performed in order to ensure any CNT/GO residue was washed from the glassware on to the film, additionally this step could assist in washing some surfactant from the CNTs in the film.

This filtration produced films that could be attached to glass and used for light transmittance and conductivity testing or attached to the silicon substrates for device production.

2.8. CNTGO Film Attachment

Once filtered, the CNT/GO films on MCE membrane were attached to the substrates using a floatation method. This method was used to prevent damage to the DAD interlayer during device production. First, the excess MCE around the edges of the CNT/GO film was clipped away and the CNT/GO film on MCE membrane was placed in an acetone bath for 10 min until the MCE had completely dissolved, leaving a free-floating CNT/GO mat in the bath. The acetone (with dissolved MCE) was removed via pipetting until only a very thin layer of acetone remained. The bath was then refilled with acetone for a further 10 min, this was followed by three more acetone refills for 10 min each. After the fifth acetone wash it was replaced with water and the mat was allowed to float for 10 min to flush acetone from the CNT/GO matrix. This process was repeated an additional two times to ensure all acetone was removed from the bath. Note that the CNT/GO film had a very fluid shape (similar to a jellyfish) when floating in acetone but stabilised and spread into a flat mat when floating in water because of the hydrophobic nature of the CNTs. To attach the free-floating film to a substrate, it was prepared and then submerged underneath the film in the water bath. The substrate was then raised through the solvent, taking the CNT/GO film with it. The substrate can be re-submerged to properly align the film until it covers the desired area. The substrate was then carefully dried under a low flow of nitrogen gas stream to avoid dislodging or deforming the film.

2.9. Gold Chloride Doping

Gold chloride (AuCl_3) was used to dope the CNT/GO film post device fabrication. The doping was performed by dissolving solid chloroauric acid (Sigma-Aldrich) in water at a concentration of 5 mM. The resultant pale-yellow suspension was dropped onto the film and left for 30 s before spin-coating at 5000 rpm for 30 s using a Laurell WS-400B-6NPP/LITE Spin Coater.

2.10. Solar Cell Testing

The performance of the solar cells were tested using a custom LabviewTM virtual instrument connected with a Keithley 2400 source unit. The power density of the collimated Xenon-arc light at the device surface with an AM 1.5G filter was calibrated to be 50 mW cm^{-2} by a standard unit cell (PV

Measurements, NIST-traceable certification). The power conversion efficiencies (PCE) are reported for the standard 100 mW cm^{-2} light intensity. The calibrations undertaken to allow this conversion are provided in the Supplementary Information.

Following a test of the “as prepared” cells, the SWCNT film was doped using gold chloride and J/V curves were then produced from the doped cells.

2.11. Characterization

SEM images were taken of DAD films formed using different spin rates and/or different deposition volumes. To achieve all SEM images, an Inspect FEI F50 SEM (Hillsboro, OR, USA) was used with beam spot size and high voltage adjusted to optimize the image quality. The image resolution was generally 2048×1768 with an imaging speed of $30 \mu\text{s}$. The SEM was calibrated using silicon calibration grids (Bruker model numbers PG: $1 \mu\text{m}$ pitch, 110 nm depth and VGRP: $10 \mu\text{m}$ pitch, 180 nm depth).

An issue with SEM imaging of thin films is that unless they exhibit a degree of surface roughness, their presence can often be hard to detect as they will appear visually similar to a bare substrate. To overcome this issue, it was decided to manually damage the film either via light scratching with a scalpel or using the laser beam in a Raman microscopy system. The scalpel will remove any polymer layer present on the surface but will have no effect on the much denser silicon underneath. These scratches were useful for AFM imaging to determine film thickness. In the case of the laser-based removal of material, the laser was focussed on the DAD film producing a spectrum with large silicon peaks accompanied by significant noise interference. Over time, the noise reduced to become negligible. At this point, the laser was stopped as it was interpreted that a clean silicon spectrum indicated that essentially all the DAD in the laser area was burnt from the surface. The laser used to remove material was from a Witec alpha300R Raman microscope (Witec, Ulm, Germany) at an excitation wavelength of 532 nm using a $\times 40$ objective with a numerical aperture of 0.60 . The power level used was to remove material and was the maximum available on the system which was approximately 30 mW .

Atomic force microscopy (AFM) was performed on solution-processed interlayers on solar device substrates to image the morphology of the films. The thickness of the solution-processed interlayers was measured using AFM by imaging the channels formed in the film with the scalpel, the height of which could be measured from cross sections using the section tool in the analysis software which allows determination of the thickness of the film. Alternatively, thickness could be determined using the depth analysis function in the AFM software and allows an analysis of the height distributions in the images where the level of the substrate and the top of the films could be determined to allow determination of film thickness.

AFM was performed in air using a Bruker multimode 8 AFM with Nanoscope V controller, operating in standard tapping mode. The AFM probes used were silicon HQNSC15/AlBS Mikromasch probes (nominal tip diameter and spring constant is 16 nm and 40 N m^{-1} respectively). Set-point, scan rate, and gain values were chosen to optimize image quality. The AFM scanner was calibrated in x , y , and z directions using silicon calibration grids (Bruker model numbers PG: $1 \mu\text{m}$ pitch, 110 nm depth and VGRP: $10 \mu\text{m}$ pitch, 180 nm depth). AFM topography images have been flattened and thickness measurements taken using Nanoscope Analysis 1.4.

Photoelectron spectroscopy in air (PESA) measurements were conducted using an AC-2 photoelectron spectrometer (Riken-Keiki Co., Tokyo, Japan).

3. Results

SEM images of the DAD films on device substrates were collected. In many cases, the images simply showed a flat topography not unlike that of the bare substrate. As such, to prove the presence of the film, the layer was intentionally damaged and imaged again. In this case, the laser approach to damage the films was used to ablate small holes in the layers. These images are provided in Figure 2. This clearly demonstrates that the film has been successfully deposited. A fuller set of both optical and SEM images are provided in the Supplemental Materials in Figures S2 and S3.

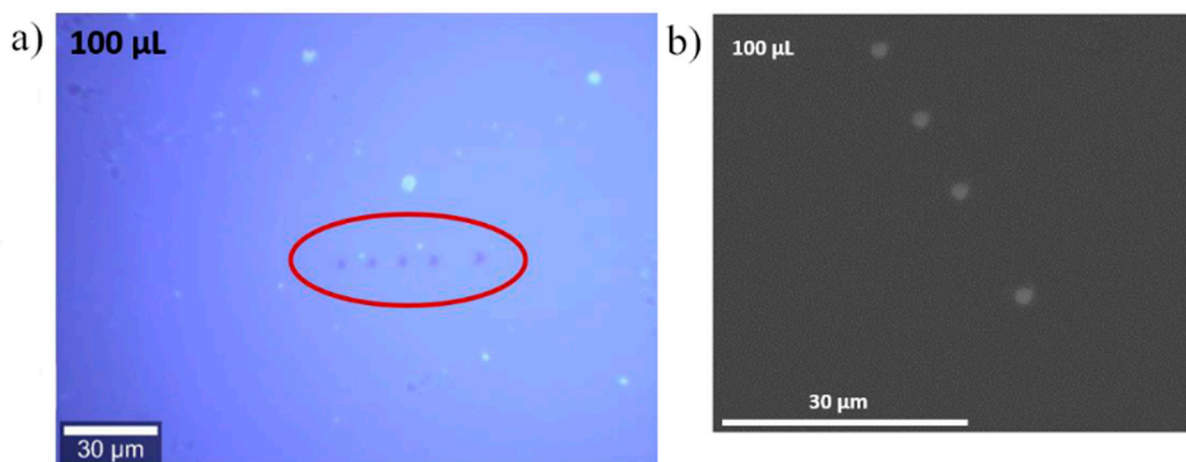


Figure 2. (a) Optical microscope image of DAD film spun from a 100 μL volume. The blue areas are the DAD film and the small white dots are air bubble holes in the film. The dark dots in the red ellipse are the burnt holes; (b) SEM image of holes in the DAD film spun from a 100 μL volume. In both cases a spin speed of 5000 rpm was used.

From the SEM images in Figure 3, it is apparent that the volume of solution spun on the surface has an effect on the film morphology. Lighter coloured regions are visible on the films. They are larger and more frequent in the 100 μL film than in the 200 μL film and there are none visible at all in the 300 μL sample. It is apparent that a volume of at least 300 μL is required to produce a smooth homogenous film. The light-coloured regions are likely thinner areas of film.

Figure 4 shows the images used to determine the thickness of the DAD layers. A fuller set of data is provided in the supplementary information for films made with different solution volumes and different spin speeds (Figures S4–S7). Across the range of volumes used (100 mL to 300 mL) and spin speeds (500 rpm to 7500 rpm), the change in film thickness observed is relatively small. All films appear to have thicknesses in the range of 10–20 nm. Our previous work has shown that this thickness range is ideal as an interlayer. If the layer is thinner, it will typically not be complete which will lower the ability to help with the charge transfer while thicker layers will push the CNTs too far away from the Si and hence the establishment of the heterojunction will be compromised.

From the PESA measurements shown in Figure 1b, the oxidation potential was measured and the HOMO value of DPA–ANT–DPA was estimated to be -5.46 eV [9]. The optical properties of the layers made using different spin speeds were measured with uv-vis spectroscopy and the data is provided in Figure S8. At higher spin speed the films do have less optical density indicating that they are getting thinner. The changes in absorbance from 500 rpm to 7500 rpm are on the order of 40% again suggesting that the thickness of the layers is not changing dramatically which is in line with the observation from the AFM measurements.

Figure 5 provides representative J/V curves for the control cells and cells with the DAD interlayer while Table 1 provides a summary of the device performance prepared with various suspension volumes. The addition of DAD has a significant effect on the performance of the devices. The data shows that a volume of 200 μL is optimal to produce the best performing devices as they outperformed the other sets across all parameters. The 150- μL set was the worst performing. However, when the J_{sc} trend is observed, it is clear that there is still a general trend of improvement with volume up until the 200 μL point. The drop-in performance for the 150 μL devices is due to concurrent drops in V_{oc} and FF. The J_{sc} displays the clearest trend, with a peak at 200 μL . Additionally, the 200 μL samples displayed the highest consistency within the device set.

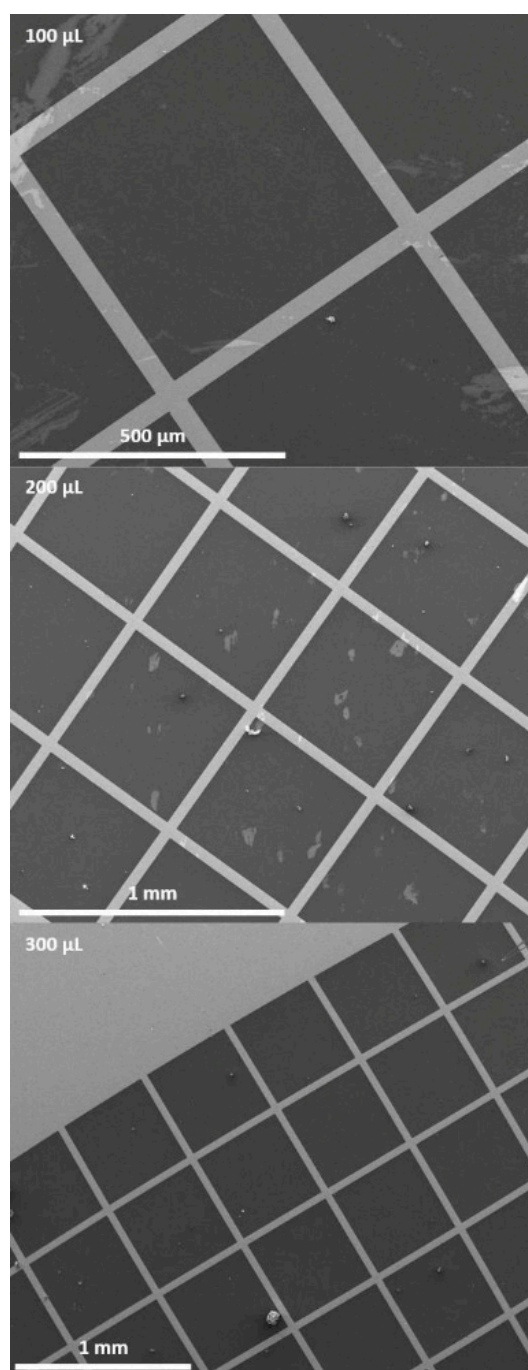


Figure 3. Larger area SEM images of DAD films spun from different solution volumes. A spin speed of 5000 rpm was used for all films.

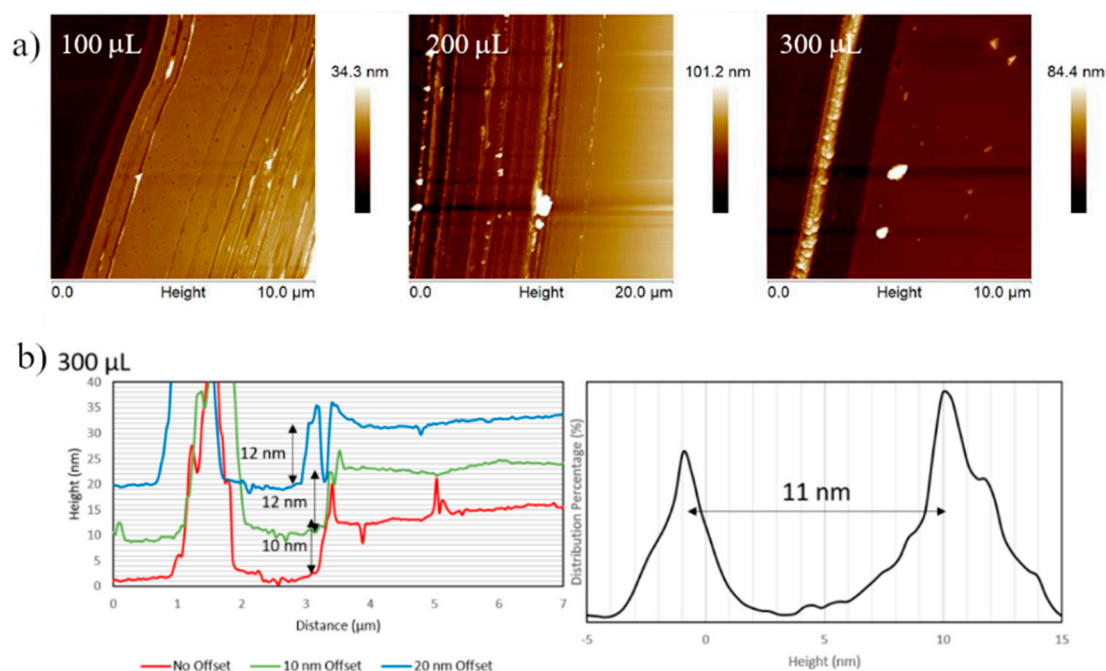


Figure 4. (a) Atomic force microscopy (AFM) height maps of DAD films spun from different solution volumes. A spin speed of 5000 rpm was used for all films; (b) representative AFM cross sectional line graphs (each cross section is off set for clarity), and percentage height distribution plots of DAD films spun from a 300 μL volume at 5000 rpm.

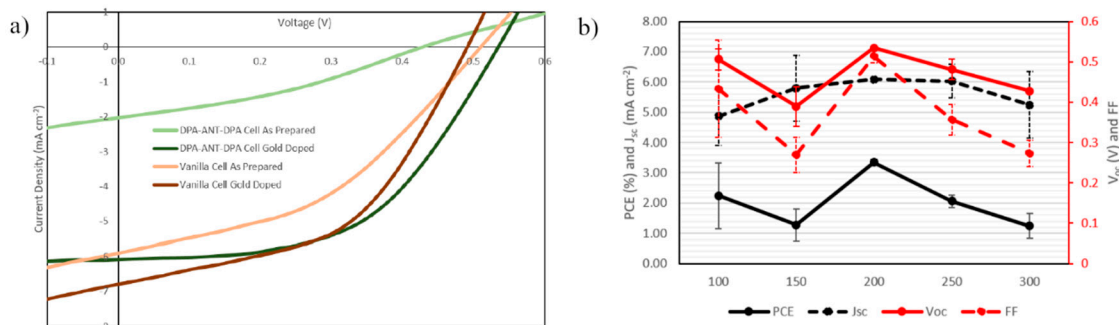


Figure 5. (a) J/V curves for the best performing device with and without a DAD interlayer; (b) J/V properties for devices with DAD interlayers spun from different solution volumes after an aqueous AuCl₃ treatment.

Table 1. Device properties of gold chloride doped devices at different DAD volumes vs devices with no interlayer.

| | PCE (%) | V _{oc} (V) | J _{sc} (mA cm ⁻²) | FF |
|-----------------|-------------|---------------------|--|-------------|
| Control Devices | 2.89 ± 0.40 | 0.48 ± 0.02 | 6.65 ± 0.30 | 0.45 ± 0.04 |
| 100 μL | 2.24 ± 1.09 | 0.51 ± 0.03 | 4.87 ± 0.97 | 0.43 ± 0.12 |
| 150 μL | 1.28 ± 0.53 | 0.39 ± 0.05 | 5.80 ± 1.09 | 0.27 ± 0.04 |
| 200 μL | 3.34 ± 0.10 | 0.53 ± 0.00 | 6.09 ± 0.02 | 0.51 ± 0.02 |
| 250 μL | 2.06 ± 0.20 | 0.48 ± 0.03 | 6.03 ± 0.55 | 0.36 ± 0.04 |
| 300 μL | 1.24 ± 0.41 | 0.43 ± 0.00 | 5.24 ± 1.09 | 0.27 ± 0.03 |

Table 1 shows that the optimal volume of 200 μL outperforms devices with no interlayer by almost 0.50% PCE (14% relative improvement). This is due to an improved V_{oc} from 0.47 ± 0.02 V to 0.53 ± 0 V and a significantly improved FF from 0.38 ± 0.10 to 0.51 ± 0.02. It is interesting to note

that the J_{sc} is actually lower in the devices with a DAD interlayer than in the devices with no interlayer. However, the difference is less than 1 mA cm^{-2} in values in the neighbourhood of 6 mA cm^{-2} and thus it can be seen that the enhancements in V_{oc} and FF outweigh the decrease in J_{sc} .

The J/V curves for the best performing device with DAD and without are shown in Figure 4a. These curves show the difference in effect of the AuCl_3 dopant on the devices. For the device with no interlayer, the AuCl_3 improved the J_{sc} from 5.90 to 6.79 mA cm^{-2} (a 15.1% improvement), improved the FF from 0.42 to 0.49 and lowered the V_{oc} from 0.51 to 0.49 V. Overall this produced a PCE gain from 2.52 to 3.24% (a 28.6% improvement). The changes exhibited in the device with a DAD interlayer were far more pronounced. The J_{sc} improved from 2.03 to 6.08 mA cm^{-2} (a 200% improvement) while the FF increased from 0.34 to 0.53 and the V_{oc} increased from 0.43 to 0.53 V. Giving an overall PCE improvement of 0.59 to 3.44% (a 483% improvement). After AuCl_3 doping, the parameters for the device with the DAD interlayer are superior to the device with no interlayer, with the exception of the J_{sc} . This matches the comparison seen between the average values (Table 1). Additionally, the deviation in PCE values was much smaller for the devices with the DAD interlayer than in those without, $\pm 0.10\%$ vs. $\pm 0.66\%$. This clearly indicates that the addition of a DAD HTM improves the performance of the large area CNT/Si heterojunction solar device.

The improvement because of the AuCl_3 treatment is largely due to an improvement in conductivity of the CNTs layer after the doping. The sheet resistance of CNTGO films before doping was $580 \pm 5 \Omega/\text{sq}$ and $199 \pm 7 \Omega/\text{sq}$ after doping. The improvement in conductivity is well established and due to the deposition of Au nanoparticles on the CNTs although the anions in the solution are thought to play a role as well [13,14]. Similar effects with Pt spheres have been observed [15]. This effect should be very similar with and without the DAD present. However, there does seem to be an extra enhancement with the interlayer present. This could be due to a modification of the DAD layer upon exposure to the AuCl_3 . Uv-vis spectroscopy shown in Figure S9 shows that there is very little change in the optical properties of the layer, and it is unlikely that the improvements are due to higher transmittances of the interlayer leading to more light reaching the silicon. The mostly likely reason for the extra improvement in performance is that the presence of the liquid for a short period makes the CNT/DAD interface somewhat “fluid” and components in the two layers can shift slightly leading to better contacts at the interface.

The smoothest and most homogenous film (Figure 3, 300 μL) is not the one that gives the best device performance. The existence of the lighter coloured regions appears to be required to improve device performance as the homogeneous films formed with a 300 μL suspension did not produce the best performing devices. The reason for this could be that the thinner regions allow a better CNT/Si junction to be formed. Thus, the peak in PCE for different DAD volumes is a trade-off between having enough thin areas in the DAD film to allow CNT/Si junction formation whilst the film being homogeneous enough to improve charge carrier extraction.

The improvement in performance for the cells after the addition of a DAD interlayer is due to two main reasons. The first is that the DAD layer will form a conformal covering on the silicon surface, whereas sparse CNT networks limit the overall photoactive junction interfacial area because of a smaller area with intimate contact between the p-type and n-type material. Addition of the CNTs onto a softer DAD layer will allow the CNTs to imbed in the layer proving better contact thus making charge transport more efficient. This encapsulation of the CNTs by the DAD layer is enhanced in the doping step which sees further device performance improvements. The second important consideration is the energy levels shown in Figure 6 [9]. The DFT-calculated energy levels differ slightly from the experimental values because of the gaseous state assumptions. CNTs are ambipolar and hence can conduct both holes and electrons. This means the CNTs are potential sites for recombination of charge carriers which will significantly lower the efficacy of the solar cells. Thus, any steps to limit the transport of one type of charge carrier into the CNT layer can improve the device performance. It is clear from past studies that a thin oxide layer is ideal for optimizing photovoltaic performance in CNT/Si devices [16]. The DAD layer limits the movement of electrons into the CNTs while improving hole

transport and is much easier to control than oxide growth so it represents an important development in maximizing the efficiencies of the CNT/Si solar cells.

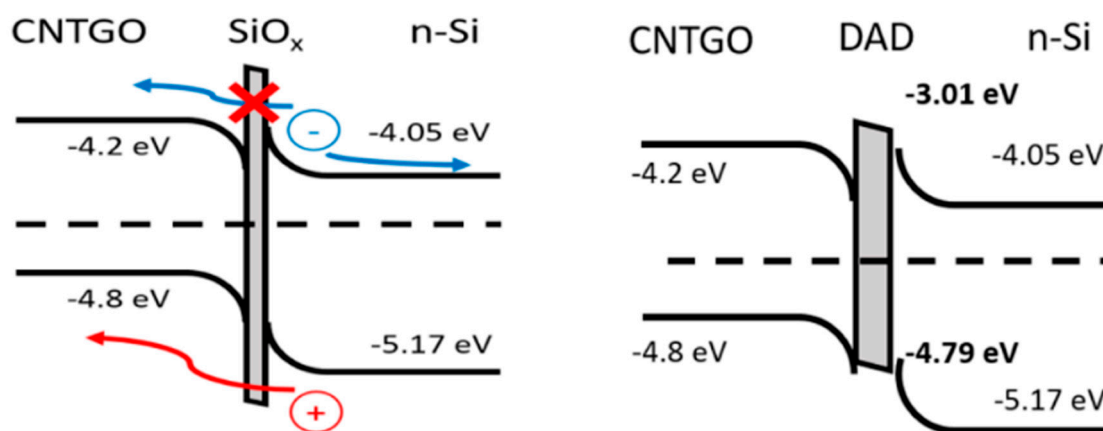


Figure 6. Energy diagrams for CNT/Si heterojunction solar devices with and without a DAD interlayer.

4. Conclusions

Overall, it is clear that a well formed homogenous DAD interlayer serves to improve device performance by providing gains in FF and in V_{oc} . It was also determined that $AuCl_3$ improved the performance of the CNTGO film in the device with the DAD layer more than the improvement observed when the CNTGO layer is in isolation. As prepared DAD containing devices vastly underperformed as prepared devices with no interlayer but the devices approached parity and beyond with the application of $AuCl_3$.

Supplementary Materials: The following are available online at <http://www.mdpi.com/2076-3417/9/21/4721/s1>. Figure S1. Effect of changing input power on photovoltaic properties in the silicon reference device and a CNT/Si device. The input power is a percentage of the optimal power of 100 mW cm^{-2} . Figure S2. Optical microscope images of DAD films spun from different solution volumes. The blue areas are the DAD films, the large white areas are gold grid lines, and the small white dots are air bubble holes in the film. The dark dots are burnt holes. Figure S3. SEM images of DAD films spun from different solution volumes. Figure S4. AFM height maps of DAD films spun from different solution volumes. Figure S5. AFM cross sectional line graphs and percentage height distribution plots of DAD films spun from different solution volumes. Figure S6. AFM height maps of DAD films spun at different speeds. Figure S7. Cross-sectional line graphs and height distribution plots for DAD films spun at different spin speeds. Figure S8 (a) UV/Visible spectra of DAD films on glass spun from $200 \mu\text{L}$ aliquots dropwise for a variety of spin speeds. (b) Peak-baseline absorbance difference vs. spin speed of DAD films on glass. Figure S9. UV/Vis spectra of 2500 rpm DAD films on glass before and after exposure to $AuCl_3$ used in the devices for doping of the CNT layer.

Author Contributions: T.G. and H.D.P. carried out the investigations and undertook the data analysis. C.T.G. also undertook some data analysis. P.S. and J.G.S. conceptualized and supervised the project and were also responsible for funding acquisition. T.G. and J.G.S. were responsible for the writing—original draft preparation while all authors were involved in writing—review and editing.

Funding: This research was funded by the AUSTRALIAN RESEARCH COUNCIL, grant number DP150101354 and DP160101301.

Acknowledgments: T.G. acknowledges Flinders University for its financial support in the form of a Research Higher Degree Scholarship during his study in Australia. The support of the Australian Research Council Discovery Program (DP150101354 and DP160101301) is gratefully acknowledged. We acknowledge the use of the South Australian nodes of Microscopy Australia (formerly known as the Australian Microscopy & Microanalysis Research Facility) and the Australian National Fabrication Facility (ANFF) at Flinders University.

Conflicts of Interest: The authors declare no conflict of interest.

References

1. Wei, J.; Jia, Y.; Shu, Q.; Gu, Z.; Wang, K.; Zhuang, D.; Zhang, G.; Wang, Z.; Luo, J.; Cao, A.; et al. Double-Walled Carbon Nanotube Solar Cells. *Nano Lett.* **2007**, *7*, 2317–2321. [[CrossRef](#)] [[PubMed](#)]

2. Wang, F.; Kozawa, D.; Miyauchi, Y.; Hiraoka, K.; Mouri, S.; Ohno, Y.; Matsuda, K. Considerably improved photovoltaic performance of carbon nanotube-based solar cells using metal oxide layers. *Nat. Commun.* **2015**, *6*, 6305. [[CrossRef](#)] [[PubMed](#)]
3. Li, X.; Lv, Z.; Zhu, H. Carbon/Silicon Heterojunction Solar Cells: State of the Art and Prospects. *Adv. Mater.* **2015**, *27*, 6549–6574. [[CrossRef](#)] [[PubMed](#)]
4. Cui, K.; Maruyama, S. Multifunctional graphene and carbon nanotube films for planar heterojunction solar cells. *Prog. Energy Combust. Sci.* **2019**, *70*, 1–21. [[CrossRef](#)]
5. Yu, L.; Tune, D.D.; Shearer, C.J.; Shapter, J.G. Application of polymer interlayers in silicon–carbon nanotube heterojunction solar cells. *ChemNanoMat* **2015**, *1*, 115–121. [[CrossRef](#)]
6. Yu, L.; Batmunkh, M.; Grace, T.; Dadkhah, M.; Shearer, C.; Shapter, J. Application of a hole transporting organic interlayer in graphene oxide/single walled carbon nanotube–silicon heterojunction solar cells. *J. Mater. Chem. A* **2017**, *5*, 8624–8634. [[CrossRef](#)]
7. Luo, Q.; Zhang, Y.; Liu, C.; Li, J.; Wang, N.; Lin, H. Iodide-reduced graphene oxide with dopant-free spiro-OMeTAD for ambient stable and high-efficiency perovskite solar cells. *J. Mater. Chem. A* **2015**, *3*, 15996–16004. [[CrossRef](#)]
8. Jena, A.K.; Numata, Y.; Ikegami, M.; Miyasaka, T. Role of spiro-OMeTAD in performance deterioration of perovskite solar cells at high temperature and reuse of the perovskite films to avoid Pb-waste. *J. Mater. Chem. A* **2018**, *6*, 2219–2230. [[CrossRef](#)]
9. Pham, H.D.; Hayasake, K.; Kim, J.; Do, T.T.; Matsui, H.; Manzhos, S.; Feron, K.; Tokito, S.; Watson, T.; Tsoi, W.C.; et al. One step facile synthesis of a novel anthanthrone dye-based, dopant-free hole transporting material for efficient and stable perovskite solar cells. *J. Mater. Chem. C* **2018**, *6*, 3699–3708. [[CrossRef](#)]
10. Yu, L.; Grace, T.; Pham, H.D.; Batmunkh, M.; Dadkhah, M.; Shearer, C.; Sonar, P.; Shapter, J. Application of Hole-Transporting Materials as the Interlayer in Graphene Oxide/Single-Wall Carbon Nanotube Silicon Heterojunction Solar Cells. *Aust. J. Chem.* **2017**, *70*, 1202–1211. [[CrossRef](#)]
11. Yu, L.; Tune, D.; Shearer, C.; Shapter, J. Heterojunction Solar Cells Based on Silicon and Composite Films of Graphene Oxide and Carbon Nanotubes. *ChemSusChem* **2015**, *8*, 2940–2947. [[CrossRef](#)] [[PubMed](#)]
12. Marcano, D.C.; Kosynkin, D.V.; Berlin, J.M.; Sinitskii, A.; Sun, Z.; Slesarev, A.; Alemany, L.B.; Lu, W.; Tour, J.M. Improved Synthesis of Graphene Oxide. *ACS Nano* **2010**, *4*, 4806–4814. [[CrossRef](#)] [[PubMed](#)]
13. Kim, S.M.; Kim, K.K.; Jo, Y.W.; Park, M.H.; Chae, S.J.; Duong, D.L.; Yang, C.W.; Kong, J.; Lee, Y.H. Role of Anions in the AuCl₃-Doping of Carbon Nanotubes. *ACS Nano* **2011**, *5*, 1236–1242. [[CrossRef](#)] [[PubMed](#)]
14. Kim, K.K.; Bae, J.J.; Park, H.K.; Kim, S.M.; Geng, H.-Z.; Park, K.A.; Shin, H.-J.; Yoon, S.-M.; Benayad, A.; Choi, J.-Y.; et al. Fermi Level Engineering of Single-Walled Carbon Nanotubes by AuCl₃ Doping. *J. Am. Chem. Soc.* **2008**, *130*, 12757–12761. [[CrossRef](#)] [[PubMed](#)]
15. Dao, V.-D.; Kim, S.-H.; Choi, H.-S.; Kim, J.-H.; Park, H.-O.; Lee, J.-K. Efficiency Enhancement of Dye-Sensitized Solar Cell Using Pt Hollow Sphere Counter Electrode. *J. Phys. Chem. C* **2011**, *115*, 25529–25534. [[CrossRef](#)]
16. Tune, D.D.; Flavel, B.S.; Krupke, R.; Shapter, J.G. Carbon Nanotube-Silicon Solar Cells. *Adv. Energy Mater.* **2012**, *2*, 1043–1055. [[CrossRef](#)]

